Available online at www.sciencedirect.com
ScienceDirect
Journal of the European Ceramic Society 28 (2008) 2213–2220
www.elsevier.com/locate/jeurceramsoc

Analyzing indentation stress–strain response of $LaGaO_3$ single crystals using spherical indenters

Siddhartha Pathak [a,*], Surya R. Kalidindi [a], Christine Klemenz [b], Nina Orlovskaya [c]

[a] Department of Materials Science and Engineering, Drexel University, 3141 Chestnut Street, LeBow 344, Philadelphia, PA 19104, USA
[b] Advanced Materials Processing and Analysis Center, University of Central Florida, Orlando, FL 32816, USA
[c] Department of Mechanical, Materials, and Aerospace Engineering, University of Central Florida Orlando, FL 32816, USA

Received 5 September 2007; received in revised form 22 January 2008; accepted 8 February 2008
Available online 2 April 2008

Abstract

In this work, a new approach to spherical nanoindentation analyses has been described and utilized to study the anisotropy of mechanical properties for (1 0 0) and (0 0 1) $LaGaO_3$ single crystals. Unlike sharp indenters, indentations by spherical indenters permit the nanoindentation load–displacement curve to be converted more reliably into indentation stress–strain curves. Using a new definition of indentation strain, we present indentation stress–strain curves that are relatively insensitive to the radii of the indenters. These curves allow the modulus of the sample to be evaluated from the elastic loading segment, instead of the common practice of approximating it from the elastic unloading segment. These measurements indicate that the (1 0 0) $LaGaO_3$ single crystal has a higher modulus and a higher hardness compared to the (0 0 1) sample.

Keywords: Nanoindentation; Perovskites; Mechanical properties; Hardness; Modulus; $LaGaO_3$

1. Introduction

Mechanical properties of the lanthanum gallate-based perovskites have received limited attention with most of the reports being concentrated on the polycrystalline ceramics[1] which yields only average properties.[2] In our previous work,[3] the anisotropy in the mechanical properties of (1 0 0) and (0 0 1) $LaGaO_3$ single crystals (the indentation direction being perpendicular to the (1 0 0) and (0 0 1) planes) was studied with respect to their micro-hardness, fracture toughness and crack propagation behavior when indented with sharp indenters (Vickers and cube corner indenter). Sharp indenters produce much higher stress and strain in the vicinity of contact which results in production and propagation of well defined cracks around the hardness impression.[4] Although this feature enables the determination of fracture toughness,[5] it is a major drawback in studying the elastic behavior of the material. On the other hand, the stress field for a spherical indenter is well defined and does not exhibit the stress singularities inherent in the sharp indenters. This makes the spherical indenters an attractive option in that they enable one to follow the entire evolution of damage modes from initial elasticity, the initiation of plasticity at a critical load (yield behavior in the form of elastic limit) to full plasticity.[6] An added advantage in using spherical indenters is that they can be used to generate indentation stress–strain curves, using certain idealizations.[7,8]

$LaGaO_3$ has been shown to be orthorhombic (*o*) *Pnma* at ambient temperature[9] and to undergo a first order phase transition to a rhombohedral (*r*) $R\bar{3}c$ structure at 145 °C.[10] Pressure can also control the relative stability of these two phases.[11] Increase in pressure should reduce the volume of the cell. In the case of $LaGaO_3$, the volume of the high temperature *r* phase is smaller than the low-temperature *o* phase. Thus at room temperature, the *r* phase is stabilized under higher pressure while releasing the pressure stabilizes the *o* phase. It has been shown that at the hydrostatic pressure of 2.5 GPa the *r* structure exists at room temperature with small amount of residual *o* phase.[11] Above 2.5 GPa, only the *r* $R\bar{3}c$ phase was reported. Upon pressure release at 1.83 GPa the reversible transition occurred and predominantly *o Pnma* phase together with a small amount of the *r* $R\bar{3}c$ phase was found. At pressures below 1.83 GPa, only the *o Pnma* phase was reported.

In this article, the calculation and analysis of indentation stress–strain curves obtained during nanoindentation by spheri-

* Corresponding author. Tel.: +1 267 243 9492; fax: +1 215 895 6760.
E-mail address: sp324@drexel.edu (S. Pathak).

0955-2219/$ – see front matter © 2008 Elsevier Ltd. All rights reserved.
doi:10.1016/j.jeurceramsoc.2008.02.009

cal diamond indenters are discussed and a comparison is made for the results obtained for (1 0 0) and (0 0 1) $LaGaO_3$ single crystals. The possibility of a phase transition in $LaGaO_3$ under the indenter due to indentation pressure is also examined.

2. Experimental details

Nanoindentations were carried out using a nanoindenter (MTS XP® System) with a 13.5 μm and a 1 μm radius spherical diamond tip. The tests were carried out under load control to peak loads of 2, 5, 8, 10, and 25 mN with the 1 μm radius spherical diamond tip and to loads of 15, 25, 50, 75, 100, 125, 150, 200, 250 and 300 mN with the 13.5 μm radius spherical diamond tip. Similar tests were carried out in aluminum, fused silica and tungsten with known values of Young's moduli, and these were used to validate the analyses procedures described below.

A micro-Raman spectrometer (Renishaw 1000) was used to identify the existence of orthorhombic and rhombohedral phases in the $LaGaO_3$ single crystals. The 514.5 nm wavelength of a green Ar^+ laser with a generated power of 12.5 mW was used to excite the samples. The laser was focused through a 100× optical objective which allowed a spot size as low as 1–2 μm. Raman spectra were collected from different points of interest on the sample surface, such as on the undeformed surface and inside Vickers impression. The micro-hardness impressions were made on the sample surface using a Vickers micro-hardness tester (LECO M-400)[3] with a load of 9.8 N. The total collection time of a single spectrum was 1–2 min. High temperature experiments were performed using the Linkam 600 hot stage. The $LaGaO_3$ samples were heated from room temperature to 300 °C with a 1 °C/min heating/cooling rate. Raman spectra were collected at 200 °C with a dwell time of 15 min. Before collection of spectra, the spectrometer was calibrated with a Si standard using a Si band position at 520 cm^{-1}. The data was analyzed using Grams 32 software.

3. Nanoindentation stress and strain

Because of the severe heterogeneity of the stress and strain fields under the indenter, the analyses of the measured load–displacement curves in nanoindentation requires considerable attention if we are to reliably extract material properties from these measurements.[12] One starts by considering the penetration of a rigid spherical indenter into a flat specimen assuming a linear elastic, isotropic, material response. For frictionless contact, Hertz's model[13] provides the solution for this simple case and is usually expressed as

$$P = \frac{4}{3}E^* R^{1/2} h^{3/2} \tag{1}$$

where h is the penetration depth caused by the indentation load P, R is the indenter radius, and E^* denotes the effective Young's modulus of the indenter and the specimen system. For a rigid indenter the effective modulus is given by the modulus and Poisson's ratio of the sample. If the indenter is assumed to behave as an elastic solid, the effective modulus is usually expressed as

$$\frac{1}{E^*} = \frac{1-\nu_s^2}{E_s} + \frac{1-\nu_i^2}{E_i} \tag{2}$$

where ν is the Poisson's ratio, E is the Young's modulus, and the subscripts s and i refer to the specimen and the indenter, respectively.

However, the sample seldom behaves in a purely elastic manner especially under the influence of the highly localized stress field under the indenter (see the schematics presented in Fig. 1a and b). In the loading segment, the sample typically experiences significant levels of inelastic strains in addition to the elastic strains. Moreover, the very small initial elastic loading segment is often not clearly identifiable in the measured load–displacement curves obtained on majority of the samples. However, in the unloading segment, the sample is likely to experience essentially elastic unloading, at least in the initial part of the unloading segment. It has been a common practice in literature to apply the Hertz's model to the unloading segment of the measured load–displacement curves,[14–16] where it is typically noted that reloading at the same spot often produces the exact same load–displacement curve as that measured in the unloading segment. Note however that this reloading is no longer from a flat surface. Rigorous methods have been proposed in literature to account for the shape of the residual indentation on the reloading curve,[17,18] by establishing an equivalent indenter shape. However, a number of studies in the literature[8,19] have generally assumed that the error introduced by ignoring this correction is relatively small.

Applying Hertz's model to the unloading segment of the measured load–displacement curve in nanoindentation permits an estimation of the Young's modulus. For this purpose, it is convenient to recast Eq. (1) as[15]

$$E^* = \frac{\sqrt{\pi}}{2}\frac{S}{\sqrt{A}} \tag{3}$$

where S is the slope of the unloading curve (i.e. dP/dh_e with h_e representing the elastic depth of indentation from the unloaded residual indent; see Fig. 1) at or close to the peak indentation load, and A is the projected contact area defined as

$$A = \pi a^2 \tag{4}$$

The radius of contact a (see Fig. 1) can be expressed as

$$a = \sqrt{2h_c R - h_c^2} \tag{5}$$

where h_c is the distance from the circle of contact to the maximum penetration depth (see Fig. 1).

In order to employ the above set of equations and extract Young's modulus of the sample, one needs the value of h_c. The Oliver and Pharr method proposes the following expression for the computation of h_c[20]:

$$h_c = h_t - \frac{1}{2}h_e = h_t - \frac{3}{4}\frac{P}{S} \tag{6}$$

Although the above equation can be applied to any point in the unloading load–displacement curve, it is customary to apply it

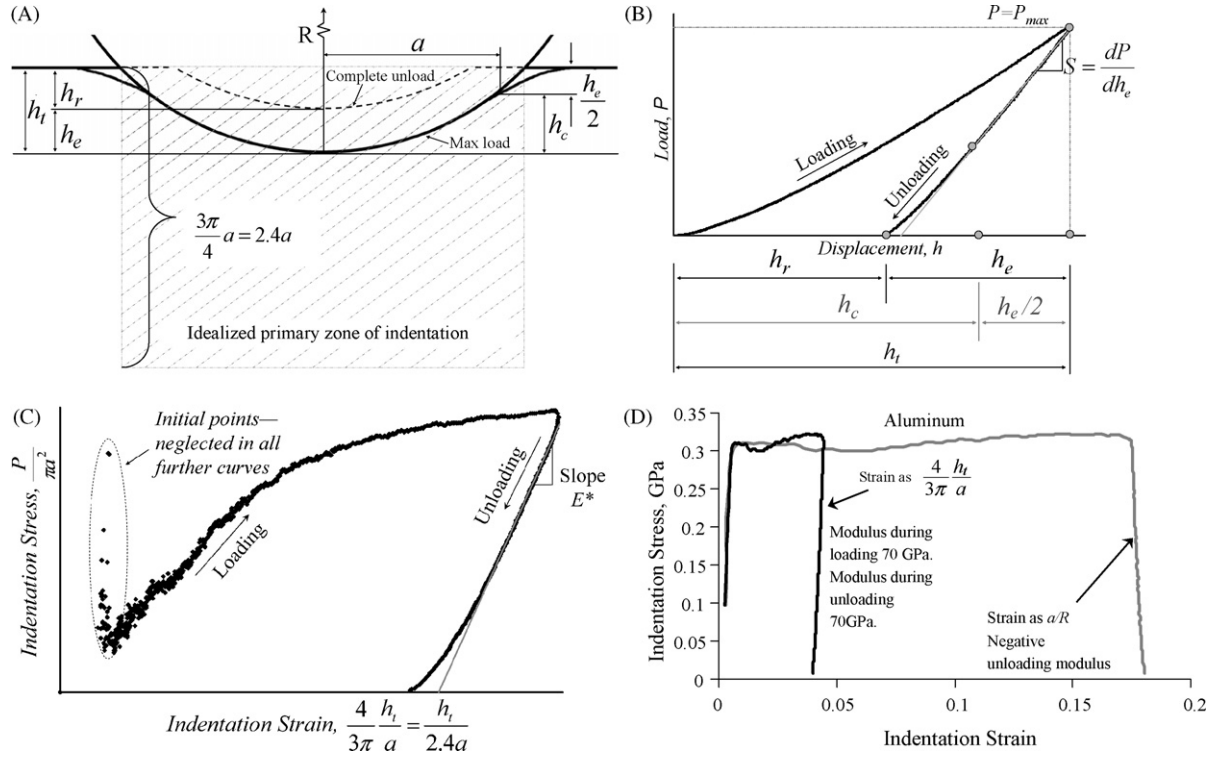

Fig. 1. (a) Schematic of contact between a rigid indenter of radius R and a flat specimen. At maximum load the depth of penetration below the specimen free surface is h_t and the radius of the circle of contact is a. $h_e/2$ is the depth of the circle of contact from the specimen free surface and h_c is the distance from the circle of contact to the maximum penetration depth. At complete unload there is a residual impression of depth h_r. Here $(3\pi/4a) = (2.4a)$ is taken to be the effective zone of indentation. (b) Typical load–displacement obtained from the nanoindenter (MTS XP® System) and (c) corresponding calculated indentation stress–strain curve. In computing the stress–strain curves, $P/\pi a^2$ was taken as the indentation stress and $(4/3\pi)h_t/a$ as the indentation strain. (d) Indentation stress–strain curves for pure aluminum obtained with the two different definitions of indentation strain. Note that the slope of the unloading curve with indentation strain = a/R is actually negative giving rise to highly unreasonable values of elastic modulus calculated from that slope. On the other hand, if we use $(4/3\pi)(h_t/a) \approx (h_t/2.4a)$ as our indentation strain, the elastic modulus during both loading and unloading correspond to the expected value (70 GPa) for aluminum.

at or close to the peak indentation load, because this is where the sample is likely to be exhibiting a purely elastic response.

In order to produce the indentation stress–strain plots, the indentation stress and the indentation strain are defined such that Eq. (1) transforms into a linear relationship as[8,19]

$$\sigma_{\text{ind}} = \frac{4E^*}{3\pi}\varepsilon_{\text{ind}}, \quad \sigma_{\text{ind}} = \frac{P}{\pi a^2}, \quad \varepsilon_{\text{ind}} = \frac{a}{R} \tag{7}$$

Note that the Eq. (7) is completely equivalent to Eq. (1) in the regime of small indentation depths (i.e. $h_c \ll R$) typical of elastic behavior. These spherical indentation stress–strain curves can be highly advantageous in identifying the elastic moduli, the indentation yield points (denoting the end of elasticity and beginning of plasticity), as well as the post-yield characteristics in the tested samples. Note that the elastic moduli can be calculated both for the elastic loading and the unloading segments when using the spherical indentation stress–strain curves.

In the plots presented in this paper, we have adopted a new definition of indentation strain. Eq. (1) has been recast here using a new definition of indentation strain as

$$\sigma_{\text{ind}} = E^*\varepsilon_{\text{ind}}, \quad \sigma_{\text{ind}} = \frac{P}{\pi a^2}, \quad \varepsilon_{\text{ind}} = \frac{4}{3\pi}\frac{h_t}{a} \tag{8}$$

The following remarks are offered to motivate and justify the definition adopted in Eq. (8) for the indentation strain:

1. The use of a/R as the indentation strain produces unrealistic values of Young's moduli for the unloading portions of the computed indentation stress–indentation strain curves for several materials. For example, in case of aluminum, the slope of the unloading stress–strain curve and hence the modulus (calculated using a/R as the indentation strain) is actually negative (Fig. 1d). We have encountered this problem of highly unrealistic unloading slopes in the analyses of spherical indentation data from numerous other materials.[21]
2. The conventional definition of strain involves the ratio of change in length over its initial length in a selected region of the sample. The proposed definition of indentation strain, $(4/3\pi)(h_t/a) \approx (h_t/2.4a)$, is tantamount to idealizing the indentation deformation as shown in Fig. 1a and b. Here it is assumed that a cylindrical region of radius a and length $2.4a$ is contracted by height h (the indentation depth) as a result of the indentation. The cylinder might expand laterally to accommodate this contraction in height. The lateral expansion is, however, not relevant to the definition of the indentation strain. This interpretation is much more physical than the definition of indentation strain as a/R, because this cannot be interpreted as change in length over its initial length in any part of the sample. Furthermore R is not an appropriate length scale characterizing the deformation caused by the indentation (a already carries that information). The main

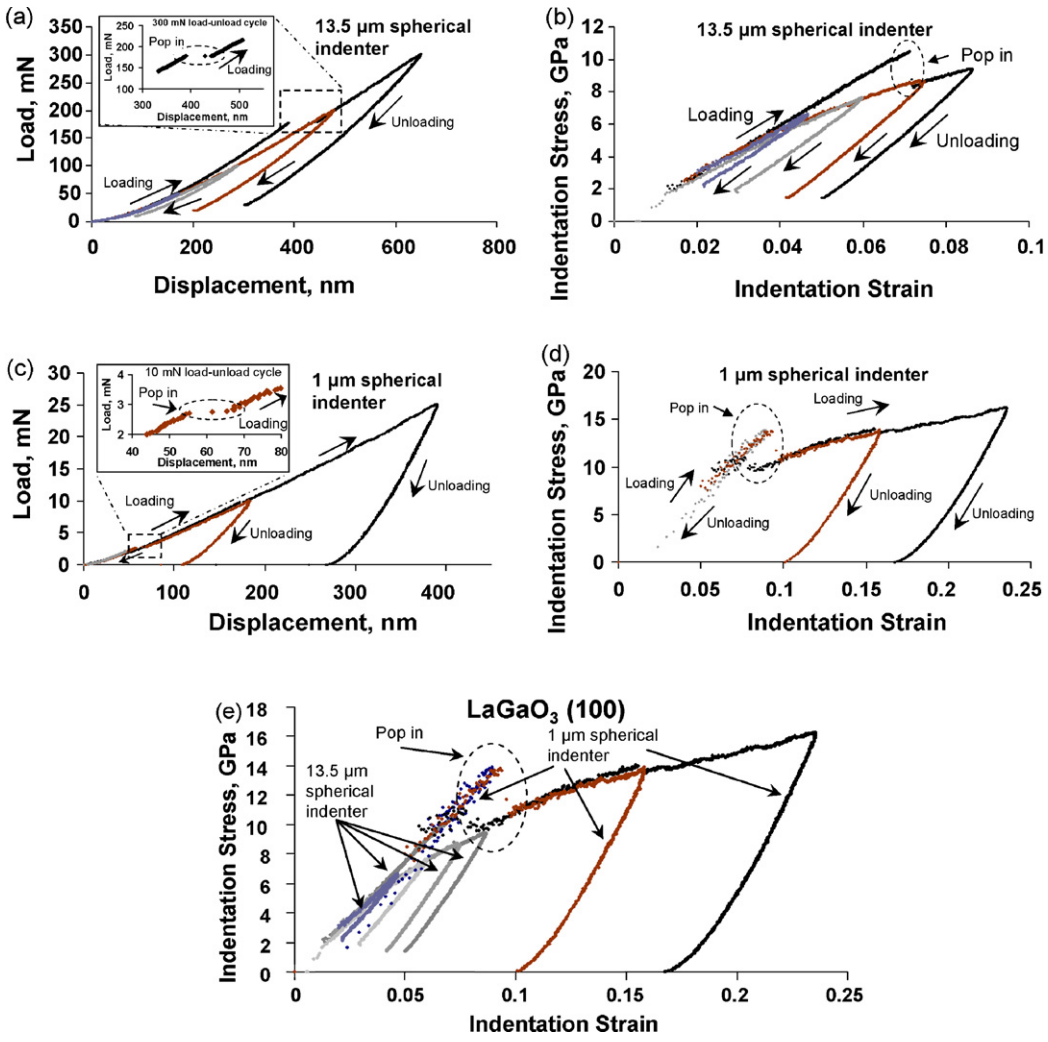

Fig. 2. Nanoindentation of (1 0 0) $LaGaO_3$ single crystal: (a) load–displacement and (b) indentation stress–strain curves for nanoindentation loads of 50, 100, 200 and 300 mN with a 13.5 μm diamond tipped spherical indenter. The insert in (a) shows the pop-in effect on the load displacement curve for a load of 300 mN. (c) Load–displacement and (d) indentation stress–strain curves for nanoindentation loads of 2, 10 and 25 mN with a 1 μm diamond tipped spherical indenter. The insert in (c) shows the pop-in event on the load–displacement curve for a load of 10 mN. This kind of pop-in is observed at load levels of 3 mN and is seen as a discontinuity in the indentation stress–strain curve. (e) Overlapped indentation stress–strain curves for both 1 and 13.5 μm indenters. The continuity of the curve between the two indenters of different diameters proves that this method is consistent for indenters of different radii.

reason for using a/R is its convenient appearance in Eq. (7). However, it will be shown next that the proposed definition is just as good for satisfying the Hertz's model for the case of a purely elastic material.

3. In the limit of small indentation depths that are typical of a purely elastic response of the sample, it can be seen that $(h_t/a) \approx (a/R)$. This implies that the definition of the indentation strain adopted here is equivalent to the definition used in the literature except for the multiplicative factor. The inclusion of this factor in the definition of the indentation strain results in the slope of the indentation stress–indentation strain curve being directly equal to the effective modulus. Whereas the definition used in Eq. (7) results in a slope of the indentation stress–indentation strain plot that needs to be corrected by a factor to produce the Young's modulus. Note that both these definitions are completely equivalent in terms of satisfying Hertz's model, except that the terms are grouped differently. However, in practice, when applied to measured data collected from samples exhibiting elastic and inelastic deformations, the two approaches result in different indentation stress–strain curves. As noted earlier, the indentation stress–strain curves obtained from the proposed definition for indentation strain produce more realistic stress–strain curves in the unloading portions and therefore these are preferred in this paper. This approach has been rigorously validated in metals such as aluminum that exhibit very little elastic anisotropy (Fig. 1d) before using them on the $LaGaO_3$ samples. Further experimental and theoretical validations are currently underway and will be reported elsewhere.

4. Results

Contact loading in the two different crystallographic directions with a spherical indenter results in different behavior of the (1 0 0) and (0 0 1) $LaGaO_3$ samples (the indentation direction

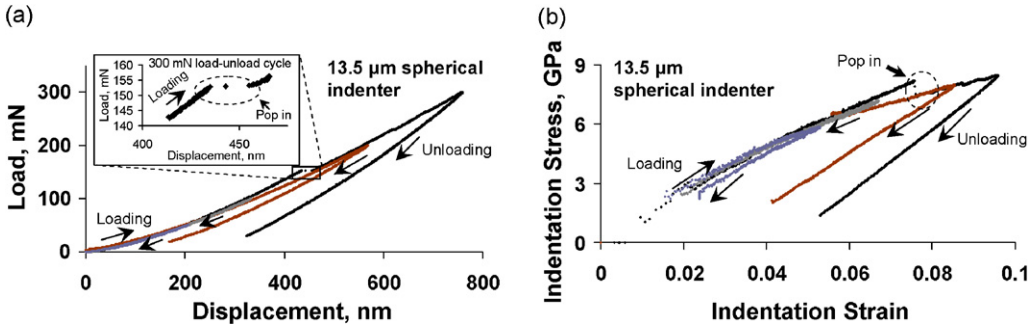

Fig. 3. Nanoindentation of (0 0 1) $LaGaO_3$ single crystal: (a) load–displacement and (b) indentation stress–strain curves for nanoindentation loads 50, 100, 200 and 300 mN with a 13.5 μm diamond tipped spherical indenter. The insert in (a) shows the pop-in effect on the load–displacement curve for a load of 300 mN.

being perpendicular to the (1 0 0) and (0 0 1) planes, respectively). The load–displacement plots obtained as a result of spherical nanoindentation were converted to their corresponding indentation stress–strain curves using Eq. (8). The indentation stress–strain curves for the (1 0 0) $LaGaO_3$ single crystal obtained by indentation with the 13.5 μm diamond spherical indenter are shown in Fig. 2a and b. The same for the 1 μm diamond spherical indenter are shown in Fig. 2c and d. Different load levels of 50, 100, 200 and 300 mN for the 13.5 μm indenter and 2, 10 and 25 mN for the 1 μm indenter are shown here as typical examples of the material behavior.

The interesting feature of these plots is the pop-in events which are observed for both the indenter sizes. Pop-in events in nanoindentation are described as abrupt increases in the penetration depth at a critical load. The associated indentation stress–strain curve show the pop-ins as a discontinuity in the curve, where the indentation stress values before the pop-in event are considerably higher than the rest of the curve while immediately after the pop-in the indentation stress value drops down to the level of stress deformation without such discontinuity.

It should be noted here that although the pop-ins with the 13.5 μm diamond spherical indenter are stochastic events, the same for the smaller 1 μm indenter were always observed to occur at a critical load, before which the deformation is essentially elastic and after which the behavior is elastoplastic. For the (1 0 0) $LaGaO_3$ single crystal the pop-ins (Fig. 2a inset and b) were observed in some cases at ∼10.4 GPa stress level (∼180 mN load) when using the 13.5 μm spherical indenter. For the 1 μm spherical indenter in the same material, the pop-ins were found to occur regularly at indentation stresses of around 13.8 GPa (2.7 mN load level). At a lower stress of 13.5 GPa (2 mN load) no pop-ins were observed, even during repeated load–unload cycles. In Fig. 2c inset, a pop-in event is shown in the loading part for the 10 mN load–unload cycle. Fig. 2d shows the associated indentation stress–strain curve for this pop-in as well as the one associated with the 25 mN load–unload cycle.

Similar behavior is observed in case of indentation of the (0 0 1) $LaGaO_3$ single crystals (Fig. 3a and b) with the 13.5 μm spherical indenter. In case of a pop-in event in this sample, the indentation stress level before the pop-in can rise to ∼8.2 GPa which decreases to ∼7.5 GPa after the pop-in. The indentation stress levels after the pop-in event are the same as those curves without any pop-in discontinuity.

The most important feature of the indentation stress–strain curves are that they allow us to evaluate the modulus of the sample from the loading portion itself (using Eq. (8)), where the slope of the curve during loading is the effective modulus. Using conventional nanoindentation analyses techniques one would evaluate the modulus using the Oliver–Pharr method [20] (Eq. (2)–(6)). It should be noted here that the Oliver–Pharr method uses the unloading portion of the curve to compute the modulus values. Both of these values are computed and compared as a function of the maximum indentation stress in Fig. 4. The modulus values for $LaGaO_3$ (1 0 0) contains the values measured by

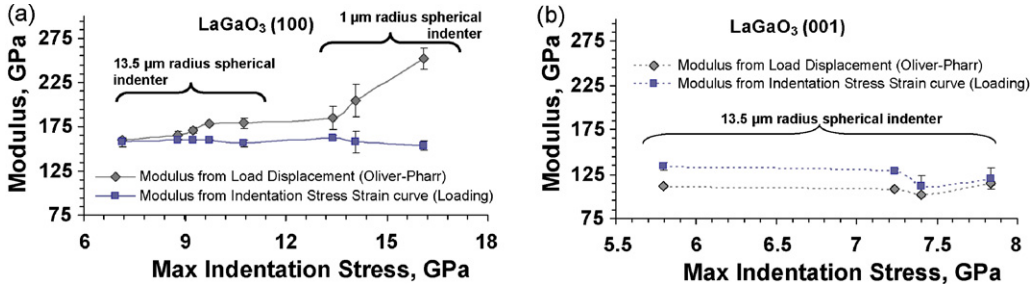

Fig. 4. Young's Modulus values for (a) the (1 0 0) $LaGaO_3$ single crystal as a function of the maximum indentation stress and (b) the (0 0 1) $LaGaO_3$ single crystal. The modulus values have been measured both from the loading portion of the indentation stress strain curves and by the Oliver–Pharr method, which measures the modulus during unloading. The (1 0 0) $LaGaO_3$ single crystal was indented with both 1 and 13.5 μm spherical indenters while only the 13.5 μm indentation tests were performed on the (0 0 1) $LaGaO_3$ single crystal.

both the 13.5 and 1 μm spherical indenters (Fig. 4a) whereas the values for $LaGaO_3$ (0 0 1) are shown only for the larger 13.5 μm spherical indenter (Fig. 4b).

As seen from Fig. 4a, the modulus values for $LaGaO_3$ (1 0 0) show a different trend depending upon whether it has been measured during loading or unloading, especially for the 1 μm spherical indenter. The modulus values measured from the loading portion of the indentation stress–strain curve are more or less constant (158.45 ± 2.7 GPa) irrespective of the maximum indentation pressure (or the indenter radius). However, the modulus values measured from the unloading portion of the load displacement curve by using the Oliver–Pharr method[20] can be seen to increase with increasing maximum indentation stress. In general, the two modulus values are similar till a maximum stress of ~9 GPa after which the modulus values during unloading are higher than those during loading for the $LaGaO_3$ (1 0 0) single crystal. This difference increases with increase in the maximum indentation stress and is significant in the stress levels of 13–16 GPa, which are the typical indentation stress levels experienced by this material under the smaller 1 μm spherical indenter.

The modulus values for the $LaGaO_3$ (0 0 1) single crystal are lower than the (1 0 0) single crystal. This corresponds to the lower K_R values for the (0 0 1) $LaGaO_3$ single crystals compared to the (1 0 0), as reported in ref.[3] Since only the larger 13.5 μm spherical indenter was used for the (0 0 1) $LaGaO_3$ single crystal, the maximum indentation stresses achieved in this sample are considerably less (~7.8 GPa). Up to this stress level, the modulus values during loading and unloading are more or less similar (as in the previous case for the (1 0 0) $LaGaO_3$ single crystal), with the values measured from the loading portion of the indentation stress–strain curve being slightly higher than the values measured from the unloading portion of the load displacement curve (using the Oliver–Pharr method).

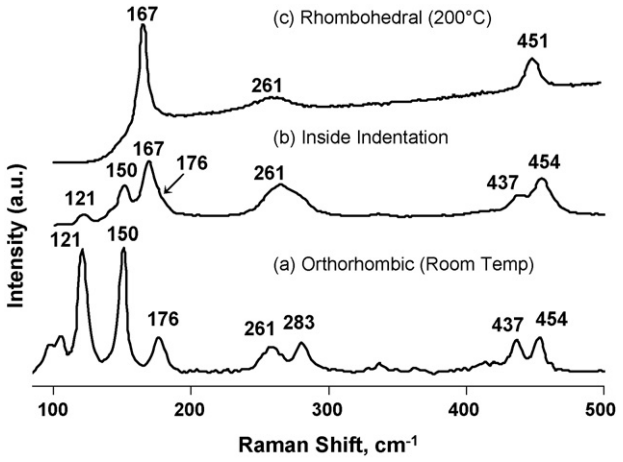

Fig. 5. Raman spectra of $LaGaO_3$ single crystal collected (a) from the polished (1 0 0) $LaGaO_3$ surface at room temperature representing the *o* (orthorhombic) phase; (b) from the surface deformed due to indentation pressure inside Vickers indentation which represents a mixture of the *o* and *r* (rhombohedral) phases and (c) collected from the undeformed surface after heating the single crystal to 200 °C which represents the *r* phase. $LaGaO_3$ single crystal is reported to undergo a first order phase transition from *o* to *r* structure at 145 °C[10].

The typical Raman spectra for the $LaGaO_3$ single crystal under different conditions of temperature and pressure are shown in Fig. 5. The spectrum shown at the bottom of Fig. 5 (spectrum a) was collected from the polished (1 0 0) $LaGaO_3$ surface. This corresponds to the room temperature *o* phase for the $LaGaO_3$ single crystal. Spectrum (b) was collected from inside Vickers impression while spectrum (c) shows the typical Raman response of undeformed $LaGaO_3$ after heating to 200 °C. Since this temperature is well above the $o \rightarrow r$ transition temperature (145 °C[10]) for the $LaGaO_3$ crystals, spectrum (c) corresponds to the high temperature *r* phase.

5. Discussion

The justification for the use of the new definitions in the indentation stress–strain curves used in the present paper (Eq. (8)) is probably best exemplified in Fig. 2e. In this figure, the indentation stress–strain curves for the two different indenter radii have been superimposed on top of each other for the $LaGaO_3$ (1 0 0) single crystal. And the result is a single curve which represents the material behavior as a continuous transition from elastic to plastic regimes. The consistent nature of the indentation stress–strain curves between the two different indenter radii provides us with a full range of material behavior from low to significantly high (~17 GPa) indentation stresses. If an observer is provided with only Fig. 2e (without the benefit of Fig. 2a–d) the curves in this figure would seem to be the indentation stress–strain plots for a single indenter loaded to different maximum stress levels and then unloaded. It should be remembered here that nanoindentation suffers from the well-known problem of defining the exact moment of first contact between the indenter and sample. Thus the indentation stress–strain curves for the 1 μm spherical indenter alone cannot give us the full stress range; the initial part of the indentation stress–strain curve would be uncertain in such a case (Figs. 1c and 2d). Thus, in a sense, this method of defining indentation stress and strain gives us back the missing information of the material behavior at the lower stress levels.

The occurrence of pop-ins in the $LaGaO_3$ (1 0 0) single crystal during indentation by both the 1 and 13.5 μm spherical indenters are also aptly described by these indentation stress–strain curves. Pop-ins, which are generally seen as abrupt increases in the penetration depth at a critical load, are manifested as discontinuities in the indentation stress–strain curves where the indentation stress drops significantly after the pop-in. When the indentation stress–strain curves from the two different indenters are superimposed, all the curves that have pop-ins display similar behavior irrespective of the indenter size. In all these curves, the material exhibits purely elastic behavior prior to the pop-in. Similar pure elastic behavior before pop-in has also been observed during nanoindentation testing of $BaTiO_3$ single crystals.[22] In the case where the sample is loaded to a load level lower than that required to cause the pop-in (for the 2 mN load–unload cycle using the 1 μm spherical indenter, Fig. 2c–d), the indentation stress–strain curve shows almost complete elastic behavior where the unloading curve retraces the loading part. These features indicate that the processes occurring under the indenter

which lead to pop-in are same in both cases, even though the pop-ins for the larger 13.5 μm indenter are more of a stochastic occurrence.

Pop-ins in nanoindentation has been reported by many researchers. They can be caused due to a variety of reasons which include, but are not limited to, sudden nucleation of dislocations, micro-fracture, delamination, etc. Their manifestation in the nanoindentation load–displacement curves as displacement bursts (or sudden stress drops in the indentation stress–strain curves) is an indication that the contact area at pop-in increases suddenly. It is generally accepted that such a phenomenon is related to the presence of a large number of mobile dislocations after pop-in, whereas before pop-in there are either no dislocations or the few that exist are of low mobility.[23] In case of defect free single crystals these pop-ins have been associated with sudden nucleation or multiplication of dislocations where the stress values prior to pop-in are close to the theoretical lattice strength of the crystal.[24]

Some stochastic pop-in events are also noticed for the (0 0 1) $LaGaO_3$ single crystal (Fig. 3a and b) when it is indented with the larger 13.5 μm spherical indenter. As in the case with the (1 0 0) $LaGaO_3$ sample, the indentation stress–strain curve in this sample with the pop-in also exhibits elastic behavior prior to pop-in while the stress values after the pop-in drops down to the level of stresses seen by curves without any such discontinuities.

The indentation stress–strain curves for the (0 0 1) $LaGaO_3$ single crystal is generally flatter with lower stress levels than that of the (1 0 0) single crystal. The indentation yield stress (defined as the point where the indentation stress–strain curve deviates from its straight line path) is higher for the (1 0 0) crystal (around 7 GPa) than the (0 0 1) crystal (around 5 GPa). Thus, the (1 0 0) $LaGaO_3$ single crystal is considerably stiffer than the (0 0 1) crystal and is able to withstand higher stress levels for the same level of strain in the material. The higher stiffness and higher hardness values (where hardness is the indentation stress at maximum load) for the (1 0 0) crystal appear to correlate with the higher fracture toughness for the (1 0 0) crystal compared to the (0 0 1) crystal as reported in ref.[3]

As already noted above, the pop-ins with the larger 13.5 μm diamond spherical indenter were stochastic events, whereas the same for the smaller 1 μm indenter always occurred at a critical stress. Below this stress value the deformation is essentially elastic while afterwards the behavior is elastoplastic. These kind of pop-in events are expected to occur with increasing regularity above a critical stress level as the indenter tip decreases in radius. Since sharp indenters (like the Berkovich or the cube-corner indenter tips) can be viewed as spherical indenters with a very small indenter radius (all sharp indenters used in practice have a residual radius at the edge), pop-ins can be observed routinely for these indenter tips. We have observed such behavior, not shown in the current paper, for metals like tungsten and aluminum when indented with the Berkovich indenter tip. Others[23] have also reported pop-ins in materials like single crystals of tungsten and gallium arsenide at a critical load for sharp indenters.

One of the greatest assets of the spherical indentation stress strain curves is that it allows us to obtain the modulus of the sample from the initial loading itself. This value relates to the value of the modulus of the virgin material and not that of the material deformed by indentation pressure as measured by the Oliver–Pharr method during unloading. In case of the material under discussion, the $LaGaO_3$ single crystal, this difference becomes very significant since $LaGaO_3$ undergoes phase transition from the *o* to the *r* phase under pressure. The hydrostatic pressure values reported to cause the pressure-induced phase transitions in $LaGaO_3$ are around 2.5 GPa during application of pressure and 1.83 GPa during release of pressure.[11] Nanoindentation stresses shown in this paper, though not entirely hydrostatic, are considerably higher than what is needed to induce the phase transition. The maximum stress values calculated are around 17 GPa for the 1 μm spherical indenter (Fig. 2d–e) and around 9 GPa for the 13.5 μm indenter (Fig. 2b). Thus, it can be safely assumed that the *r* $R\bar{3}c$ $LaGaO_3$ phase exists at high stresses under the indenter. The appearance of the *r* phase due to indentation pressure has also been confirmed by micro-Raman spectroscopy. As seen in Fig. 5, the 167 cm^{-1} *r* band can be clearly detected inside the hardness impression (spectrum b). This is indicative of the presence of both *r* and *o* phases after contact loading, as it can be seen by comparison with spectra (a) and (c). Since a detailed discussion on the origin of the vibrational bands in the room temperature *o* phase and the high temperature *r* phase is beyond the scope of the present paper, it will be presented elsewhere.

The advantage of obtaining the modulus values from the loading portion instead of the unloading portion is evident in Fig. 4a. In this figure, the modulus values calculated from the loading portions are seen to remain constant while those from the unloading part increases with increasing maximum indentation stress. The loading portions of the indentation stress–strain curves represent the situation when the spherical indenter is pressed on to a flat surface. This problem, within elastic limits, is in agreement with the mathematical formulations presented in Eqs. (1)–(6), where the modulus is independent of the applied indentation stress. Hence, this provides us with a constant value of modulus during loading at different increasing indentation stresses. However, during unloading, we are dealing with a situation where a spherical indenter is pressed into a surface distorted by prior indentation stresses; a problem that requires significantly different treatment than the situation described in Eqs. (1)–(6). At best, these equations are a highly approximate description of this altered problem, which generates significant errors at higher stress levels. Also, as evident from the previous discussion, during unloading we might be measuring the modulus of a mixture of two phases; x % *r* phase and $(100 - x)$ % *o* phase, where x is the amount of material that has undergone phase transition with x increasing with increasing indentation pressure. Either of these two causes, or more probably a combination of both, results in increasing modulus values with increasing indentation stresses during unloading.

Since the maximum indentation stress values generated by the 13.5 μm spherical indenter during indentation on the (0 0 1) $LaGaO_3$ single crystal are comparatively much lower, such a behavior is not seen for this sample. In this case, the modulus

values for both the loading and unloading sections seem to match over the pressure range.

6. Conclusions

Nanoindentations on (1 0 0) and (0 0 1) $LaGaO_3$ single crystals have been performed using spherical indenters of 13.5 and 1 μm radii. The load displacement curves generated from the nanoindentation experiments have been converted into indentation stress–strain curves and these curves were used in analysis of the test results. A new definition of indentation strain $(4/3\pi)(h_t/a) \approx (h_t/2.4a)$ has been proposed as an improved representation of the indentation deformation. The (1 0 0) $LaGaO_3$ single crystal was found to have a higher modulus and a higher hardness value than the (0 0 1) sample. The $LaGaO_3$ samples were found to undergo an $o \rightarrow r$ phase transition under pressure during nanoindentation. The modulus values measured by conventional techniques using the Oliver–Pharr method was found to be significantly affected by increasing indentation stresses. In this respect, the modulus values measured from the indentation stress–strain curves were found to be highly consistent over a range of indentation stresses. This effect is probably due to the residual curvature on the sample surface during unloading because of the indentation stresses during loading or an $o \rightarrow r$ phase transition under pressure induced by nanoindentation or both.

Acknowledgement

This work was supported by the National Science Foundation through grant number DMR-0201770.

References

1. Baskaran, S., Lewinsohn, C. A., Chou, Y.-S., Qian, M., Stevenson, J. W. and Armstrong, T. R., Mechanical properties of alkaline earth-doped lanthanum gallate. *J. Mater. Sci.*, 1999, **34**, 3913–3922.
2. Vasylechko, L., Vashookc, V., Savytskiia, D., Senyshyna, A., Niewab, R., Knappd, M. *et al.*, Crystal structure, thermal expansion and conductivity of anisotropic $La_{1-x}Sr_xGa_{1-2x}Mg_{2x}O_{3-y}$ ($x = 0.05$, 0.1) single crystals. *J. Solid State Chem.*, 2003, **172**(2), 396–411.
3. Pathak, S., Kalidindi, S. R., Moser, B., Klemenz, C. and Orlovskaya, N., Analyzing indentation behavior of $LaGaO_3$ single crystals using sharp indenters. *J. Eur. Ceram. Soc.*, 2008, **28**, 2039–2047.
4. Hay, J. L. and Pharr, G. M., Instrumented indentation testing. In *ASM Handbook vol. 8: Mechanical Testing and Evaluation*, ed. H. Kuhn and D. Medlin. 10th ed. ASM International, Materials Park, OH, USA, 2000, pp. 232–243.
5. Swain, M. V., Mechanical property characterization of small volumes of brittle materials with spherical tipped indenters. *Mater. Sci. Eng. A: Struct. Mater. Properties Microstruct. Process.*, 1998, **253**, 160–166.
6. Lawn, B. R., Indentation of ceramics with spheres: a century after Hertz. *J. Am. Ceram. Soc.*, 1998, **81**(8), 1977–1994.
7. Barsoum, M. W., Murugaiah, A., Kalidindi, S. R., Zhen, T. and Gogotsi, Y., Kink bands, nonlinear elasticity and nanoindentations in graphite. *Carbon*, 2004, **42**(8–9), 1435–1445.
8. Field, J. S. and Swain, M. V., A simple predictive model for spherical indentation. *J. Mater. Res.*, 1993, **8**(2), 297–306.
9. Howard, C. J. and Kennedy, B. J., The orthorhombic and rhombohedral phases of $LaGaO_3$—a neutron powder diffraction study. *J. Phys.: Condens. Matter*, 1999, **11**, 3229–3236.
10. O'Bryan, H. M., Gallagher, P. K., Berkstresser, G. W. and Brandle, C. D., Thermal analysis of rare earth gallates and aluminates. *J. Mater. Res.*, 1990, **5**(1), 183.
11. Kennedy, B. J., Vogt, T., Martin, C. D., Parise, J. B. and Hriljac, J. A., Pressure-induced orthorhombic to rhombohedral phase transition in $LaGaO_3$. *J. Phys.: Condens. Matter*, 2001, **13**, L925–L930.
12. Tabor, D., *The Hardness of Metals*. Oxford University Press, 1951.
13. Hertz, H., *Miscellaneous Papers*. MacMillan and Co., Ltd, New York, 1896.
14. Fischer-Cripps, A. C., Critical review of analysis and interpretation of nanoindentation test data. *Surf. Coatings Technol.*, 2006, **200**(14–15), 4153–4165.
15. Fischer-Cripps, A. C., A review of analysis methods for sub-micron indentation testing. *Vacuum*, 2000, **58**, 569–585.
16. Radovic, M., Lara-Curzio, E. and Riester, L., Comparison of different experimental techniques for determination of elastic properties of solids. *Mater. Sci. Eng. A*, 2004, **368**(1–2), 56–70.
17. Pharr, G. M. and Bolshakov, A., Understanding nanoindentation unloading curves. *J. Mater. Res.*, 2002, **17**(Oct 10), 2260–2671.
18. Oliver, W. C. and Pharr, G. M., Measurement of hardness and elastic modulus by instrumented indentation: Advances in understanding and refinements to methodology. *J. Mater. Res.*, 2004, **19**(Jan 1), 3–20.
19. Basu, S., Moseson, A. and Barsoum, M. W., On the determination of spherical nanoindentation stress–strain curves. *J. Mater. Res.*, 2006, **21**(10), 2628–2637.
20. Oliver, W. C. and Pharr, G. M., An improved technique for determining hardness and elastic modulus using load and displacement sensing indentation experiments. *J. Mater. Res.*, 1992, **7**(6), 1564–1580.
21. Proust, G. and Kalidindi, S. R., Effect of the Crystal Orientation on the Measured Response during Nanoindentation. *TMS Letters*, 2004, **1**(7), 151–152.
22. Liu, D., Chelf, M. and White, K. W., Indentation plasticity of barium titanate single crystals: dislocation influence on ferroelectric domain walls. *Acta Mater.*, 2006, **54**(17), 4525–4531.
23. Syed, S. A. and Pethica, J. B., Nanoindentation creep of single crystal tungsten and gallium arsenide. *Philos. Mag. A*, 1997, **76**(6), 1105–1118.
24. Pethica, J. B. and Oliver, W. C., In *Stresses and Mechanical Properties. in Materials Research Society Symposium Proceedings*, 1989.